Research Papers

Enhanced power factor in CaMnO$_3$-based thermoelectric ceramics via co-doping

P. Amirkhizi [a,*] , M.A. Torres [b] , M. Depriester [c] , M. Hedayati [a] , A. Sotelo [b] , M.A. Madre [b] , A.V. Kovalevsky [a] , Sh. Rasekh [a]

[a] Department of Materials and Ceramic Engineering, CICECO-Aveiro Institute of Materials, University of Aveiro, Aveiro 3810-193, Portugal
[b] INMA (CSIC-Universidad de Zaragoza), Mª de Luna, 3, Zaragoza 50018, Spain
[c] UDSMM (EA 4476), MREI-1, Université du Littoral Côte d'Opale, Dunkerque 59140, France

ARTICLE INFO

ABSTRACT

Nb-doped Ca$_{0.97}$Y$_{0.01}$La$_{0.01}$Yb$_{0.01}$Mn$_{1-x}$Nb$_x$O$_3$ materials were prepared to assess their thermoelectric properties. Samples were obtained by sintering at 1583 K for 12 h involving planetary milled precursors. XRD analysis indicated primarily thermoelectric phase with minor CaMn$_2$O$_4$. Microstructural observations revealed decreasing grain size with increasing Nb content. However, electrical resistivity decreases for the samples with Nb-content up to 0.03, which can be associated with the increase of the charge carrier concentration. The lowest value at 1073 K (9.2mΩcm) is among the best reported in the literature. Seebeck coefficient decreased with Nb-doping, and the best PF value at 1073 K has been determined for 0.01Nb samples (~0.48mW/K^{2}m). Assuming the thermal conductivity at 1073 K similar to that at 473 K, the calculated ZT values are among the typically reported in this family. These results highlight the promise of CaMnO$_3$-based materials for integration in thermoelectric modules working under steady-state mode, where the high PF values are of great importance.

1. Introduction

The rapid growth of the world population has led to an increasing demand for energy at an alarming rate. However, traditional energy sources are limited and contribute to global warming through CO$_2$ emissions. This fact, together with their low efficiency, where about 65 % of energy used is wasted in the form of heat, drastically increases their consumption. Therefore, the search for alternative green energy sources, or increasing the efficiency of these traditional sources, has become crucial [1–3]. One promising solution for harvesting this wasted heat is the utilization of thermoelectric materials, which have the unique ability to transform heat directly into electricity. Nowadays, the field of thermoelectric materials has gained significant attention as a potential avenue for sustainable energy solutions. Although initial successes proving the viability of this technology were achieved around 1960 for tellurium bismuth alloys, only in the 21st century a substantial enhancement in thermoelectric properties of these alloys have been accomplished, provided by the advancements in technology and novel approaches [3,4]. However, the currently employed classical thermo-electric materials face two primary drawbacks. Firstly, they consist of heavy, toxic, and scarce elements, making them expensive and environmentally unfriendly. Secondly, their application at high temperatures is limited due to issues such as evaporation, oxidation, and degradation. Therefore, the search for environmentally friendly materials which are abundant, cost-effective, and capable of withstanding long periods of operation at relatively high temperatures without degradation or oxidation, has become a crucial goal.

Among the different types of thermoelectric materials, ceramic compounds have attracted considerable attention due to their high temperature stability as well as their relatively high abundance and reasonable cost [5]. In this regard, CaMnO$_3$, a perovskite-type oxide, has emerged as a highly promising material due to its unique combination of properties, including a high Seebeck coefficient and relatively low thermal conductivity. While CaMnO$_3$ exhibits interesting thermoelectric properties, still they should be enhanced to achieving a high figure of merit (ZT), which quantifies the overall efficiency of a thermoelectric material, and it is defined as ZT = TS^2/ρκ (T: absolute temperature; S: Seebeck coefficient; ρ: electric resistivity; and κ: thermal conductivity). Despite its high Seebeck coefficient and low thermal conductivity, the ZT value of CaMnO$_3$ is low due to its high electrical resistivity.

Consequently, researchers have explored various strategies to further enhance the thermoelectric properties of $CaMnO_3$. Among the different approaches, electron doping using different elements has been investigated to enhance electrical conductivity through optimising charge carrier concentration. Once elements are introduced in adequate proportions into the structure as dopants, $CaMnO_3$ displays low electrical resistivity and moderate Seebeck coefficient. Considering the sites where these dopants are introduced, these studies can be categorized into single or dual doping at A- and/ or B-site, which allow reaching ZT values between 0.2 and 0.32 [5–9].

On the other hand, previous studies have also indicated that the final properties of bulk materials are significantly influenced by preparation techniques such as coprecipitation [10–12], sol-gel [12–14], spray-drying [12,15], planetary milling [16,17], or attrition milling [18], which lead to the enhancement of thermoelectric performances due to the decrease of the precursors particle sizes, increasing their reactivity. The main goal of this work is to improve the thermoelectric performances of $CaMnO_3$ by Nb doping at the Mn-site while also using a promising co-doping approach at the Ca-site, as previously reported [19]. Taking into account the previous results, $Ca_{0.97}Y_{0.01}La_{0.01}Yb_{0.01}Mn_{1-x}Nb_xO_3$ ($x = 0$, 0.01, 0.03, and 0.05) has been selected for this study. It is expected that Nb-doping further decreases the lattice thermal conductivity already achieved with the triple substitution in the Ca site and decreases the electrical resistivity by increasing carrier concentration due to the higher oxidation state of the substituting cations. Additionally, planetary milling has been employed to reduce the initial particle size of the precursors to enhance their reactivity. This combined approach is assessed by evaluating the thermoelectric properties of the sintered materials and related structural and microstructural characteristics.

2. Experimental

For this work the $Ca_{0.97}Y_{0.01}La_{0.01}Yb_{0.01}Mn_{1-x}Nb_xO_3$ ($x = 0$, 0.01, 0.03, and 0.05) precursors were prepared from $CaCO_3$ ($\geq$ 98 %, PanReac), Y_2O_3 (99.99 %, Sigma), La_2O_3 (99 %, Panreac), Yb_2O_3 (99.9 %, Aldrich), Mn_2O_3 (99 %, Aldrich) and Nb_2O_5 (99.5 %, Alfa Aesar) commercial powders. They were weighed in the appropriate proportions and then subjected to planetary milling with the weight ratio of ball-to-powder of 2.5:1 in 20 ml of distilled water media for 4 h at 400 rpm. The milled powders were then dried at 493 K, hand-milled using a mortar and pestle (for 15 min across all samples to maintain the consistency between different samples) to break agglomerates and homogenize the particle distribution, and subjected to a two-step calcination procedure at 1223 and 1323 K for 12 h with an intermediate manual milling. All prepared powders were cold uniaxially pressed in the form of pellets ($3 \times 3 \times 15$ mm^3) under 400 MPa using polyvinyl alcohol (PVA) as binder. To remove the PVA, the pellets were placed into a furnace at 723 K for 2 h, followed by sintering at 1583 K for 12 h.

Phase identification has been performed by powder X-Ray Diffraction (XRD) analysis at room temperature, using a PHILIPS X'PERT system with CuK$_\alpha$ radiation ($\lambda = 1.5406$ Å), with 2θ between 20 and 75 degrees. Morphological and microstructural characterization of samples surfaces was performed in a field emission scanning electron microscope (FESEM Zeiss Merlin), equipped with an energy-dispersive X-ray spectrometer (EDX) used to determine the chemical composition of grains.

The density of the samples has been measured using the Archimedes' method, for several samples of each composition. Relative density has been calculated using 4.705 g/cm^3 as the theoretical density of $CaMnO_3$ [12]. Electrical resistivity and Seebeck coefficient values of all samples were simultaneously measured, using the standard DC four-probe technique, in an LSR-3 apparatus (Linseis GmbH) between 323 and 1073 K under steady-state conditions at Helium atmosphere. From the measured S and ρ values, the power factor ($PF = S^2/\rho$) values have been calculated to determine the electrical performances. Thermal conductivity has been determined using the infrared photothermal radiometry

(PTR), which measures thermal diffusivity (α) and effusivity (e), obtaining κ from $\kappa = e \sqrt{\alpha}$ [20,21] between room temperature and 473 K. For higher temperatures, a rough estimation of the thermal conductivity was assumed. Samples were cut in slices of 300 μm thickness. The thermal parameters were obtained from a data fitting of the normalized phase of the signal. For temperatures lower than 373 K, glycerol was used as a substrate and a brass substrate for temperatures beyond. Glycerol and brass substrates were used at the same operating temperature of 373 K assuring that similar thermal conductivity values were obtained with both substrates. When brass substrate is used, air gap thickness between the sample and the substrate is also a fitted parameter in addition to thermal parameters, as already suggested by Salazar et al. in a similar procedure developed for the photopyroelectric technique [22]. Hall effect measurements were performed at room temperature using an L79/HCS system (Linseis GmbH) in an air atmosphere to determine the charge carrier concentration and mobility of all samples. Finally, with the power factor and thermal conductivity, the thermoelectrical performances of samples were determined by calculating their ZT values up to 473 K, and estimated for higher temperatures.

3. Results and discussion

The results of powder XRD analysis of samples after sintering are presented in Fig. 1, for all samples (using 2θ from 20 to 50°, for clarity). These patterns reveal that the major peaks are associated with the $CaMnO_3$ phase (indicated by their diffraction planes) in all cases, with a perovskite structure (Pnma space group), as previously reported [23]. Moreover, the sharp peaks observed at different angles indicate well crystallized polycrystalline structure. Furthermore, it is clear that all samples are nearly single-phase provided by the high reactivity of precursors due to their small sizes, as a result of planetary milling. On the other hand, it is also clear that Nb is incorporated into the crystal structure, as no Nb-based secondary phases have been identified. However, very small amount of $CaMn_2O_4$ (Marokite phase) can be identified through its main peak at around 32.9°.

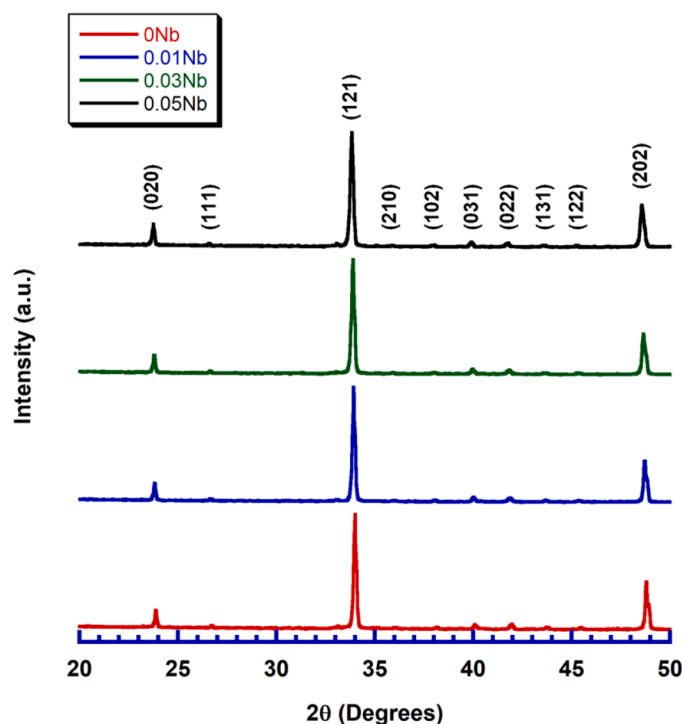This result is further confirmed when the manganite peaks are

Fig. 1. Powder XRD patterns of all samples. Diffraction planes identify the peaks associated with the manganite phase.

closely observed, as shown in Fig. 2, where an enlarged view of the (121) peak of all samples is displayed. The peak shifts to lower angles when the amount of dopant is increased due to the expansion of the unit cell provided by the larger ionic size of Nb^{5+} (0.64 Å), when compared to that of Mn^{4+} (0.53 Å).

In order to evaluate the doping effects and their influence on the evolution of cell parameters, Rietveld refinement has been performed for each sample. For this purpose, perovskite structure with the space group of Pnma (62) for the pristine $CaMnO_3$ has been considered. The results for the cell parameters for all samples are summarised in Table 1, together with their respective errors. As it can be observed in the table, the cell parameters gradually increase on increasing the Nb amount, as qualitatively observed in Fig. 2. This expansion of the unit cell with the amount of Nb confirms its integration in the structure due to its higher ionic radius (0.64 Å for Nb^{5+}) compared to the Mn^{4+} one (0.53 Å). Furthermore, the presence of Nb^{5+} promotes the partial reduction of Mn^{4+} to Mn^{3+}, with higher ionic radius (0.645 Å), to maintain electrical neutrality, contributing to the unit cell expansion. Other interesting data obtained from the analysis is the amount and nature of the secondary phase in the samples, which is quantitatively very small in all cases, confirming the observations of Fig. 1.

Fig. 3 displays representative SEM micrographs taken on the sintered surfaces of all samples. These images show that the amount of porosity decreases for low doping content ($\leq$ 0.03) when compared to the undoped one, and increases for higher content (x = 0.05). The presence of pores in the sintered samples results from multiple mechanisms, including incomplete packing of powders, gas release from binder decomposition, competition between grain growth and pore shrinkage, and the influence of dopants and secondary phases. Pores tend to become stabilized at grain boundaries if grain coarsening outpaces densification. Additionally, Nb doping appears to influence the sintering kinetics as a grain growth inhibitor, leading to higher porosity at elevated doping levels, as seen in SEM micrograph (Fig. 3d). In order to confirm these observations, the density of samples was determined through Archimedes' method, and the results are displayed in Table 2. As can be observed, these data are aligned with the SEM observations. Furthermore, it is worth mentioning that these values correspond to relative densities between 91 and 93 % of the theoretical one for the $CaMnO_3$ compound. These values are higher than the typical reported

for this family of compounds (68–89 %) [25–27], and in the order of the best published values (90–99 %) [12]. On the other hand, these micrographs indicate that grain sizes decrease when the amount of dopant is increased. This phenomenon points out to the effect of dopants on the grain size, acting as grain growth inhibitors and avoiding coarsening phenomena. This inhibition arises from the segregation of Nb^{5+} ions at the grain boundaries, which creates a pinning effect and prevents extensive grain growth. Additionally, the partial reduction of Mn^{4+} to Mn^{3+} due to charge compensation mechanisms, introduces lattice strain and potential defect formation. These defects further contribute to limiting the mobility of grain boundaries, thereby affecting the final microstructure. Another contributing factor is the presence of small amounts of $CaMn_2O_4$ secondary phases, which may form at the grain boundaries and act as barriers to grain growth. These evolutions have been confirmed by determining the mean grain sizes, together with their standard error, in several micrographs by the line intercept method [24]; the results are presented in Table 2. To provide a comparative perspective on grain size evaluation, crystallite size estimations were also performed using the Scherrer equation based on the four most intense peak. These values were obtained by fitting the peak profile with a Gaussian function to determine the full width at half maximum (FWHM), Table 2. The results show that the crystallite sizes range from ~42 to 58 nm, which are significantly smaller than the grain sizes observed by SEM. This difference confirms that the grains in these sintered ceramics are composed of multiple coherently diffracting domains.

To complement the SEM microstructural analysis and confirm the uniform distribution of elements in the samples, EDS elemental mapping was performed, and the results are shown in Fig. 4. The elemental maps clearly show that Ca, Mn, and all dopants (Y, La, Yb, and Nb) are uniformly distributed throughout the scanned area. These findings reinforce the XRD and SEM results and support the conclusion that the synthesis method enabled successful incorporation of all dopants into the perovskite matrix, ensuring local compositional homogeneity critical for reliable thermoelectric performance. Another interesting feature observed is an increase of the grain size dispersion due to the uneven grain growth in these samples. These morphological modifications are typically caused by high calcination temperatures and long sintering times. Finally, despite the identification of $CaMn_2O_4$ phase in the XRD refinement, it could not be observed in these micrographs. Previously reported data showed that the secondary phase can be produced by an intergrowth inside the thermoelectric grains [19].

To better understand the influence of Nb doping on the electronic transport properties, Hall effect measurements were performed to determine charge carrier concentration and mobility. These parameters provide further insight into the electronic transport behavior observed in the electrical resistivity and Seebeck coefficient trends. The results confirm that Nb doping significantly increases the charge carrier concentration, which directly influences the reduction in electrical resistivity and the corresponding decrease in the Seebeck coefficient. As shown in Table 3, the charge carrier concentration increases from 7.233 10^{18} cm^{-3} (x = 0) to 4.055 10^{19} cm^{-3} (x = 0.05), following the expected trend due to the Nb^{5+} substitution at the Mn-site. This substitution leads to the formation of a higher amount of Mn^{3+} facilitating the electronic hopping between Mn^{4+} and Mn^{3+}, which is the main mechanism for electronic transport in manganites [30,31].

The results of electrical resistivity measurements vs temperature for all samples are shown in Fig. 5, which align well with these findings. As it is illustrated in the graph, the Nb-free sample displays metallic-like behavior up to around 873 K, followed by a semiconducting-like behavior at higher temperatures. On the other hand, Nb-doping gradually reduces the semiconducting behavior disappearing for Nb content $\geq$ 0.03, when samples show a metallic-like behavior in the whole measured temperature range. Moreover, the electrical resistivity is much lower in these samples than in the Nb-free one, due to increased charge carrier concentration, same as previously reported [28,29]. Moreover, the lowest electrical resistivity in the whole measured
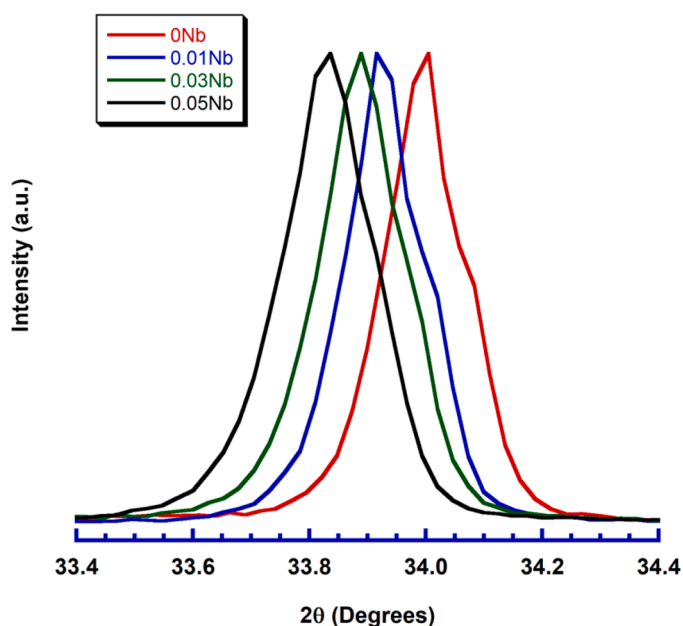

Fig. 2. Enlarged view of the XRD peak located at 2θ ∼ 34°, illustrating the peaks shift when the amount of dopant is increased.

Table 1

Calculated cell parameters of the different samples with their error, and the amount of $CaMn_2O_4$ secondary phase.

Nb	a	Error	b	Error	c	Error	Wt%($CaMn_2O_4$)
0.00	5.28924	0.00019	7.46421	0.00026	5.27289	0.00019	2.16
0.01	5.29408	0.00012	7.46736	0.00015	5.27712	0.00012	3.75
0.03	5.30149	0.00017	7.47499	0.00019	5.28186	0.00015	4.36
0.05	5.31412	0.00013	7.48753	0.00019	5.28937	0.00014	4.53
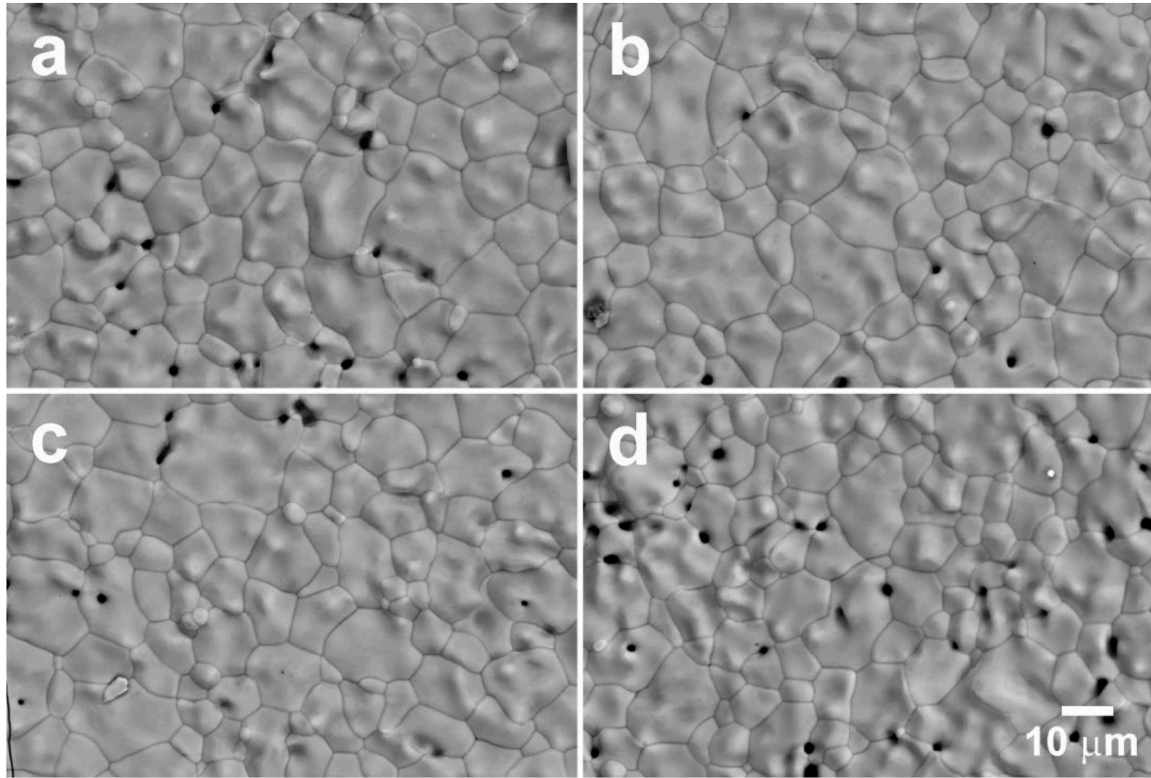
Fig. 3. Representative SEM micrographs obtained for the surface of the $Ca_{0.97}Y_{0.01}La_{0.01}Yb_{0.01}Nb_xMn_{1-x}O_3$ samples, for $x = a$) 0.0; b) 0.01; c) 0.03; and d) 0.05.

Table 2

Mean grain sizes (from SEM), together with their standard error, Scherrer-based crystallite size estimations from XRD, and absolute density values, with their standard error, determined by the Archimedes' method.

Composition $Ca_{0.97}Y_{0.01}La_{0.01}Yb_{0.01}Mn_{1-x}Nb_xO_3$	Mean grain size (μm)	Std. Error (μm)	**Crystallite size (nm)**	Density (g/cm³)	Std. Error (g/cm³)
$X = 0.00$	8.76	0.41	58	4.29	0.04
$X = 0.01$	8.54	0.34	46	4.35	0.04
$X = 0.03$	8.25	0.49	44	4.31	0.05
$X = 0.05$	7.29	0.31	42	4.27	0.03

temperature range has been measured in the 0.03 Nb-substituted samples. The lowest value measured in 0.03 Nb-doped samples at 1073 K (9.2 mΩ cm), is about 40 % lower than that determined in the Nb-free sample. Furthermore, it is among the best-reported values in the literature for sintered manganite compounds (7.5–12 mΩ cm) [32–35]. This significant reduction is primarily attributed to the increased charge carrier concentration, as confirmed by the Hall measurements. However, at $x = 0.05$, a slight increase in resistivity suggests that factors such as grain boundary scattering and defect accumulation counteract the benefits of increased carrier concentration. This effect is reflected in the Hall mobility values, which decrease from 104.644 cm²/V·s ($x = 0$) to 45.657 cm²/V·s ($x = 0.05$), indicating stronger charge carrier scattering at high Nb doping levels.

Fig. 6 depicts the behavior of the Seebeck coefficient with temperature, as a function of the sample composition, which further support these findings. As it can be seen in the graph, all the samples show a negative Seebeck coefficient in the whole measured temperature range, meaning that charge carriers conduction mechanism is governed by electrons (n-type behavior). Furthermore, as the temperature increases, the absolute Seebeck ($|S|$) values are raised, as shown in metals or degenerate semiconductors in which charge carrier concentration, effective mass, and Fermi level are constant with temperature [36]. This is mainly due to the position of the Fermi level inside or very close to the conduction band, which prevents significant thermal excitation of carriers. Similarly, the effective mass of charge carriers is a material-dependent property that remains stable across the temperature range studied. As a result, the Fermi level exhibits only a minimal shift with increasing temperature, leading to a Seebeck coefficient behavior similar to that observed in metals or degenerate semiconductors, where $|S|$ increases linearly with temperature. Moreover, $|S|$ values are decreasing when the amount of dopant is raised due to the increase of charge carrier concentration [37], as Seebeck coefficient is much less
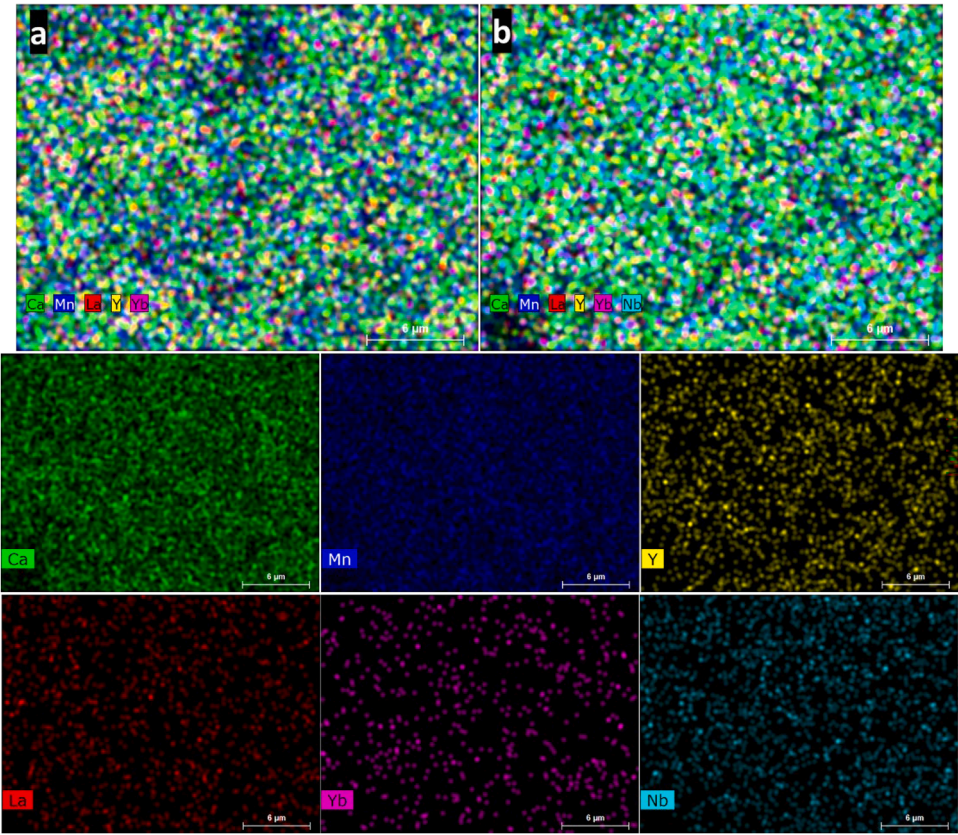
Fig. 4. Representative EDS elemental maps for the $Ca_{0.97}Y_{0.01}La_{0.01}Yb_{0.01}Nb_xMn_{1-x}O_3$ samples, (a) $x = 0.0$, (b) $x = 0.01$, and EDS maps for Ca, Mn, Y, La, Yb, and Nb.

Table 3

Charge carrier concentration and mobility of $Ca_{0.97}Y_{0.01}La_{0.01}Yb_{0.01}Nb_xMn_{1-x}O_3$ samples at room temperature, measured by Hall effect.

Nb content X	Charge concentration (cm⁻³)	Mobility (cm²/V s)
0.00	7.233×10^{18}	104.644
0.01	1.875×10^{19}	97.806
0.03	2.969×10^{19}	70.170
0.05	4.055×10^{19}	45.657

sensitive to the previously described microstructural modifications than the electrical resistivity [38], in agreement with obtained results for resistivity. Consequently, besides the Nb-free sample, the highest |S| value at 1073 K has been attained for 0.01 Nb-doped samples (224 µV/K). This value is only about 7 % lower than the obtained in the undoped samples, but it is much larger than those typically reported in this manganite family (between 64 and 160 µV/K) [32,33,39,40].

The electric performances of samples, represented by their PF, have been calculated using the previous ρ and S data and presented, vs temperature, in Fig. 7. In the graph, it is evident and expected, that increasing the temperature leads to a higher power factor, provided by the large increase of S. The highest power factor value at 1073 K has been achieved in the 0.01 Nb-doped sample due to the optimal combination of S and ρ (~ 0.48 mW/K²m). This value is approximately 20 % higher than that determined in the Nb-free sample. Moreover, it is also higher than the typical values reported in the literature for the manganites family (0.10–0.40 mW/K²m) [32,35,39,41,42].

Fig. 8 illustrates the evolution of total thermal conductivity with temperature determined for all samples between room temperature and 473 K, and the estimation at 1073 K. As it is well known, κ typically decreases with temperature in this family [7,12,29,43–46], even though some studies showed that the value at 1073 K is, approximately, the same in the whole measured temperature range [39,47–49].
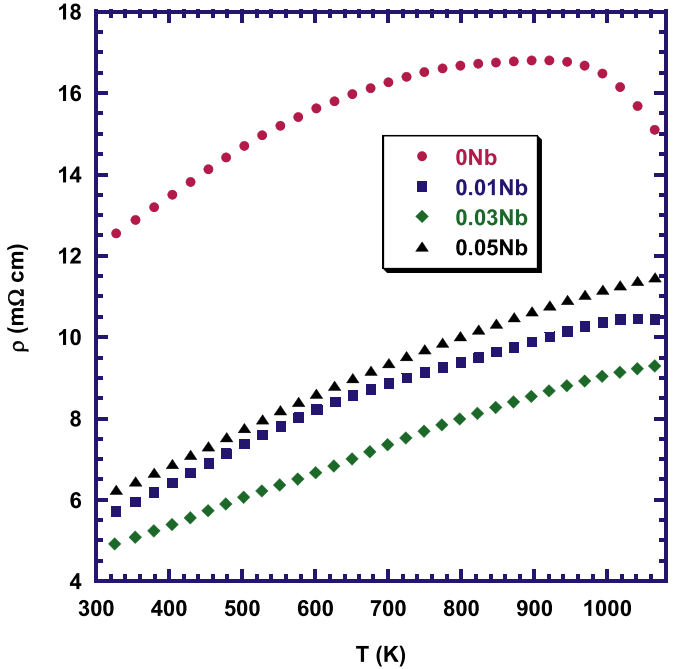

Fig. 5. Evolution of the electrical resistivity with temperature for all $Ca_{0.97}Y_{0.01}La_{0.01}Yb_{0.01}Mn_xNb_xO_3$ samples.

Consequently, for the estimation of thermal conductivity at 1073 K, the same value determined at 473 K has been used as a rough estimation. It must be noticed that most of the samples show a clear decrease of thermal conductivity with temperature. The decrease in thermal
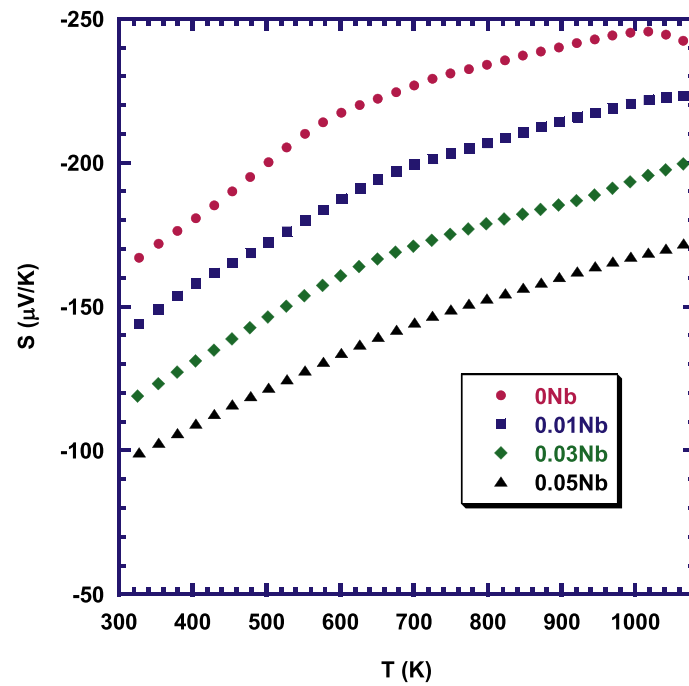
Fig. 6. Evolution of the Seebeck coefficient with temperature for all $Ca_{0.97}Y_{0.01}La_{0.01}Yb_{0.01}Mn_xNb_xO_3$ samples.
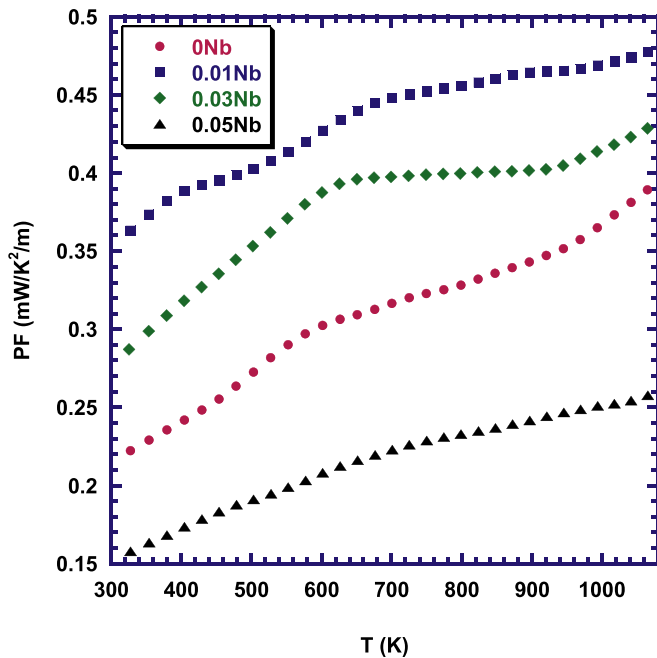
Fig. 7. Evolution of the power factor with temperature for all $Ca_{0.97}Y_{0.01}La_{0.01}Yb_{0.01}Mn_xNb_xO_3$ samples.
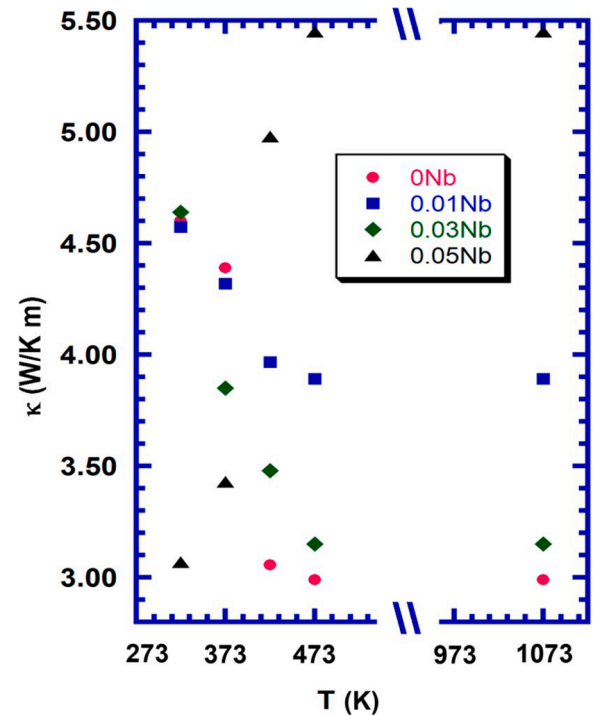
Fig. 8. Evolution of the thermal conductivity with temperature for all $Ca_{0.97}Y_{0.01}La_{0.01}Yb_{0.01}Mn_xNb_xO_3$ samples.

conductivity with increasing temperature is primarily attributed to reducing the phonon mean free path and enhanced phonon-phonon Umklapp scattering, which dominates at high temperatures and follows an inverse relationship with temperature. Additional contributions from grain boundary scattering and defect-induced phonon disruptions also contribute to lowering thermal conductivity. In doped samples, the presence of Nb further disrupts phonon transport through mass fluctuation scattering, while electron-phonon interactions become more significant at higher temperatures. These combined effects lead to the observed reduction in thermal conductivity across the measured temperature range. However, the unique thermal conductivity behaviour of

the $x = 0.05$ sample, starting with lower values at low temperatures and then increasing with temperature, can be attributed to the interplay between charge carrier concentration and phonon scattering mechanisms. As shown by the Hall effect results, the charge carrier concentration in the $x = 0.05$ sample is significantly higher (4.055×10^{19} cm^{-3}) compared to the lower Nb-doped samples. This higher carrier concentration leads to defect clustering and local strain in the crystal lattice, as evidenced by the reduced charge carrier mobility (45.657

cm^2/V·s). These defects act as strong phonon scatterers at low temperatures, where phonon transport is dominant, thereby lowering the lattice thermal conductivity. Additionally, the smaller grain size and higher porosity further enhance phonon scattering at grain boundaries, further reducing the thermal conductivity at low temperatures. However, as the temperature increases, the efficiency of phonon scattering may decrease due to saturation effects, allowing for a more significant electronic contribution to the overall thermal conductivity. According to the Wiedemann-Franz law ($\kappa_e \propto \sigma T$), the electronic thermal conductivity increases with both temperature and charge carrier concentration, leading to the observed rise in total thermal conductivity in the $x = 0.05$ sample at elevated temperature. Taking into account these considerations, the minimum estimated thermal conductivity for the doped samples at 1073 K has been found in the 0.03 Nb-doped samples (3.15 W/K m), which is slightly higher than that of the undoped ones. On the other hand, it is similar to the reported for classically prepared samples (3.1 W/K/m) [29,43], but much higher than the typically reported for this family of materials (1.1–2.9 W/K m) [7,12,39,44–49] probably due to the overestimation of thermal conductivity at 1073 K.

The observed variations in electrical conductivity, Seebeck coefficient, and thermal conductivity with Nb doping could be understood through charge transport models for degenerate semiconductors. The electrical resistivity decrease is attributed to increased charge carrier concentration from Nb^{5+} substitution, while the Seebeck coefficient reduction follows the expected inverse relationship with carrier concentration. The decrease in thermal conductivity is primarily due to enhanced phonon scattering mechanisms, including Umklapp processes and defect-induced scattering. These findings highlight the potential of Nb-doped CaMnO$_3$ as an efficient n-type thermoelectric material, with an optimal doping level at $x = 0.03$ to balance electrical and thermal transport properties.

The overall thermoelectric performances of samples were calculated from the power factor and thermal conductivity data and is presented, as a function of temperature, in Fig. 9. As it can be observed in the graph, ZT shows an increasing trend with temperature, much less marked for the 0.05 Nb-substituted samples provided by their very high thermal conductivity. Moreover, the highest calculated and estimated values at 473 and 1073 K, 0.06 and 0.14, respectively, correspond to the 0.03 Nb-doped samples. These values are only slightly higher than the ones determined in Nb-free samples, probably due to the overestimation of thermal conductivity previously discussed. However, they are in the order of the typical values reported in these compounds (0.03–0.19) [12, 29,43–47,49–52], but much lower than the best compounds presented in the literature (0.20–0.44) [7,25,39,48,53,54].

In spite of the relatively low ZT values obtained in these materials, they can be considered for integration in thermoelectric modules for power generation in applications, allowing steady-state conditions, provided by their high power factor, representing the electrical production capability. In fact, the highest efficiency expressed by ZT and highest power output are usually observed at different charge carrier concentrations, leaving space for possible optimization of the desired performance, taking into account the specific conditions of the application. Thus, especially for applications at high temperatures, as in the case of the discussed materials, the power factor could be a better quality criterion as compared to ZT [55].

4. Conclusions

In this work, Ca$_{0.97}$Y$_{0.01}$La$_{0.01}$Yb$_{0.01}$Mn$_x$Nb$_x$O$_3$ materials, with $x = 0$, 0.01, 0.03, and 0.05, have been successfully prepared by the solid-state route involving the planetary milled precursors. XRD patterns showed that the main peaks correspond to the desired thermoelectric phase, and a very small amount of CaMn$_2$O$_4$ secondary phase has been identified calculated by refining the data. SEM studies demonstrate a decreasing trend for the grain sizes when the amount of dopant was increased. The microstructural evolution has affected the electrical resistivity, which is
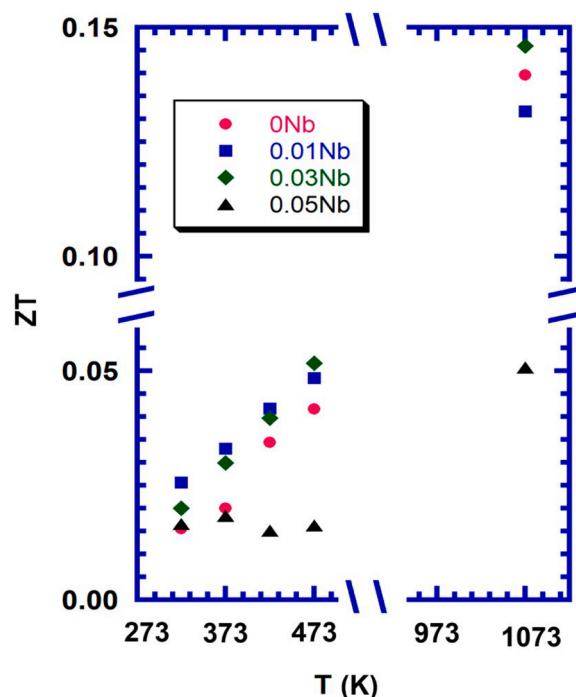

Fig. 9. Evolution of ZT with temperature for all Ca$_{0.97}$Y$_{0.01}$La$_{0.01}$Yb$_{0.01}$Mn$_x$Nb$_x$O$_3$ samples.

decreased with Nb-doping up to 0.03, increasing for higher content. The lowest resistivity at 1073 K determined in the studied samples (9.2 mΩ cm) is 40 % lower than the measured in Nb-free samples, and it is among the best reported in the literature. On the other hand, the Seebeck coefficient decreases when the amount of Nb is increased, due to the higher charge carrier concentration, in agreement with combined electrical resistivity and Seebeck observation. The highest power factor at 1073 K has been obtained in 0.01 Nb-doped samples (~ 0.48 mW/K^{2}m), which is also higher than the typical values reported in the literature for these materials. Thermal conductivity was determined up to 473 K and estimated at 1073 K considering the value obtained at 473 K. This assumption resulted in overestimation of the thermal conductivity values, which still led to ZT values within the typically reported for these materials, but far from the best ones. However, these materials appear to be promising candidates for integration in high-temperature thermoelectric modules working under steady-state mode.

CRediT authorship contribution statement

P. Amirkhizi: Writing – review & editing, Writing – original draft, Methodology, Investigation, Formal analysis. **M.A. Torres:** Software, Formal analysis, Data curation. **M. Depriester:** Writing – review & editing, Software, Investigation, Formal analysis, Data curation. **M. Hedayati:** Writing – review & editing, Methodology. **A. Sotelo:** Writing – review & editing, Writing – original draft, Validation, Supervision, Resources, Project administration, Conceptualization. **M.A. Madre:** Validation, Software, Formal analysis, Data curation. **A.V. Kovalevsky:** Writing – review & editing, Supervision, Funding acquisition, Conceptualization. **Sh. Rasekh:** Writing – review & editing, Supervision, Funding acquisition, Conceptualization.

Declaration of competing interest

The authors declare that they have no known competing financial interests or personal relationships that could have appeared to influence the work reported in this paper.

Acknowledgements

Data availability

Data will be made available on request.

References

[1] D. Champier, Thermoelectric generators: a review of applications, Energy Convers. Manage 140 (2017) 167–181, https://doi.org/10.1016/j.enconman.2017.02.070.

[2] S. Twaha, J. Zhu, Y. Yan, B. Li, A comprehensive review of thermoelectric technology: materials, applications, modelling and performance improvement, Renew. Sustain. Energy Rev. 65 (2016) 698–726, https://doi.org/10.1016/j.rser.2016.07.034.

[3] H. Ohta, Thermoelectrics based on strontium titanate, Mater. Today 10 (2007) 44–49, https://doi.org/10.1016/S1369-7021(07)70244-4.

[4] I. Terasaki, Introduction to thermoelectricity, C. C. Sorrell, S. Sugihara, J. Nowotny (Eds.). Materials for Energy Conversion Devices, Woodhead Publishing, Cambridge, 2005, pp. 339–357, https://doi.org/10.1533/9781845690815.3.339.

[5] C. Li, Q. Chen, Y. Yan, Effects of Pr and Yb dual doping on the thermoelectric properties of CaMnO3, Materials 11 (2018) 1–13, https://doi.org/10.3390/ma11101807 (Basel).

[6] J.W. Park, D.H. Kwak, S.H. Yoon, S.C. Choi, Thermoelectric properties of Bi, Nb co-substituted CaMnO3 at high temperature, J. Alloys Compd. 487 (2009) 550–555, https://doi.org/10.1016/j.jallcom.2009.08.012.

[7] X.Y. Huang, Y. Miyazaki, T. Kajitani, High temperature thermoelectric properties of Ca1-xBixMn1-yVyO3-δ (0≤x=y≤0.08), Solid State Commun. 145 (2008) 132–136, https://doi.org/10.1016/j.ssc.2007.10.012.

[8] T. Liu, J. Chen, M. Li, G. Han, C. Liu, D. Zhou, J. Zou, Z.G. Chen, L. Yang, Achieving enhanced thermoelectric performance of Ca1-x-yLaxSryMnO3 via synergistic carrier concentration optimization and chemical bond engineering, Chem. Eng. J. 408 (2021) 127364, https://doi.org/10.1016/j.cej.2020.127364.

[9] C.M. Kim, D.H. Kim, H.Y. Hong, K. Park, Thermoelectric properties of La3+ and Ce3+ co-doped CaMnO3 prepared by tape casting, J. Eur. Ceram. Soc. 40 (2020) 735–741, https://doi.org/10.1016/j.jeurceramsoc.2019.08.021.

[10] J.G. Noudem, D. Kenfaui, S. Quetel-Weben, C.S. Sanmathi, R. Retoux, M. Gomina, Spark plasma sintering of n-type thermoelectric Ca0.95Sm0.05MnO3, J. Am. Ceram. Soc. 94 (2011) 2608–2612, https://doi.org/10.1111/j.1551-2916.2011.04465.x.

[11] J. Philip, T.R.N. Kutty, Preparation of manganite perovskites by a wet-chemical method involving a redox reaction and their characterization, Mater. Chem. Phys. 63 (2000) 218–225, https://doi.org/10.1016/S0254-0584(99)00223-0.

[12] R. Lohnert, M. Stelter, J. Topfer, Evaluation of soft chemistry methods to synthesize Gd-doped CaMnO3-δ with improved thermoelectric properties, Mater. Sci. Eng. B 223 (2017) 185–193, https://doi.org/10.1016/j.mseb.2017.06.014.

[13] S.T. Aruna, M. Muthuraman, K.C. Patil, Combustion synthesis and properties of strontium substituted lanthanum manganites La1-xSrxMnO3 (0≤x≤0.3), J. Mater. Chem. 7 (1997) 2499–2503, https://doi.org/10.1039/A703901H.

[14] W. Hizi, H. Rahmouni, K. Khirouni, E. Dhahri, Nanoparticles size effect on transport properties of doped manganite elaborated by sol-gel route, J. Mater. Sci. Mater. Electron. 34 (2023) 1173, https://doi.org/10.1007/s10854-023-10573-w.

[15] H. Muguerra, B. Rivas-Murias, M. Traianidis, C. Marchal, Ph. Vanderbemden, B. Vertruyen, C. Henrist, R. Cloots, Thermoelectric properties of n-type Ca1-xDyxMn1-yNbyO3-δ compounds (x = 0, 0.02, 0.1 and y = 0, 0.02) prepared by spray-drying method, J. Alloys Compd. 509 (2011) 7710–7716, https://doi.org/10.1016/j.jallcom.2011.04.056.

[16] FAl Aziz, Masruroh, AIM. Fauzy, SP. Sakti, DJ.D.H. Santjojo;, Rotational speed effect of the planetary ball milling on the particle size and crystal structure of CaMnO3 as a thermoelectric material, AIP Conf. Proc. 2818 (1) (2023) 060006, https://doi.org/10.1063/5.0131210, 21 August.

[17] L.K. Joy, D. Singh, P.M. Sudeep, V. Ganesan, P.M. Ajayan, S. Thomas, M. R. Anantharaman, Size effect on the colossal thermoelectric power in charge ordered small band width manganites based on Gd-Sr, Mater. Res. Express 2 (2015) 055504, https://doi.org/10.1088/2053-1591/2/5/055504.

[18] A. Sotelo, M.A. Torres, M.A. Madre, J. Diez, Effect of synthesis process on the densification, microstructure, and electrical properties of Ca0.9Yb0.1MnO3 ceramics, Int. J. Appl. Ceram. Technol. 14 (2017) 1190–1196, https://doi.org/10.1111/ijac.12711.

[19] M.A. Madre, H. Amaveda, O.J. Dura, D. Pelloquin, M. Mora, M.A. Torres, S. Marinel, A. Sotelo, Effect of Y, La, and Yb simultaneous doping on the thermal conductivity and thermoelectric performances of CaMnO3 ceramics, J. Alloys. Compd. 954 (2023) 170201, https://doi.org/10.1016/j.jallcom.2023.170201.

[20] M. Depriester, P. Hus, S. Delenclos, A.H. Sahraoui, New methodology for thermal parameter measurements in solids using photothermal radiometry, Rev. Sci. Instrum. 76 (2005) 074902, https://doi.org/10.1063/1.1942532.

[21] D.P. Almond, P. Patel, Photothermal, Science and Techniques, 1st ed., Chapman & Hall, London, 1996.

[22] A.O A.Salazar, A. Mendioroz, E. Apiñaniz, Retrieving the thermal diffusivity and effusivity of solids from the same frequency scan using the front photopyroelectric technique, Meas. Sci. Technol. 28 (2017) 105011, https://doi.org/10.1088/1361-6501/aa8449.

[23] K.R. Poeppelmeier, M.E. Leonowicz, J.C. Scanlon, B. Yelon, Structure determination of CaMnO3 and CaMnO2.5 by X-ray and neutron methods, J. Solid State Chem. 45 (1982) 71–79, https://doi.org/10.1016/0022-4596(82)90292-4.

[24] X. Li, L. Cui, J. Li, Y. Chen, W. Han, S. Shonkwiler, S. McMains, Automation of intercept method for grain size measurement: a topological skeleton approach, Mater. Des. 224 (2022) 111358, https://doi.org/10.1016/j.matdes.2022.111358.

[25] L. Bocher, M.H. Aguirre, D. Logvinovich, A. Shkabko, R. Robert, M. Trottmann, A. Weidenkaff, CaMn1-xNbxO3 (x ≤ 0.08) perovskite-type phases As promising new high-temperature n-type thermoelectric materials, Inorg. Chem. 47 (2008) 8077–8085, https://doi.org/10.1021/ic800463s.

[26] C.S. Sanmathi, Y. Takahashi, D. Sawaki, Y. Klein, R. Retoux, I. Terasaki, J. G. Noudem, Microstructure control on thermoelectric properties of Ca0.96Sm0.04MnO3 synthesised by co-precipitation technique, Mater. Res. Bull. 45 (2010) 558–563, https://doi.org/10.1016/j.materresbull.2010.01.023.

[27] J. Lan, Y.H. Lin, H. Fang, A. Mei, C.W. Nan, Y. Liu, S. Xu, M. Peters, High-temperature thermoelectric behaviors of fine-grained Gd-doped CaMnO3 ceramics, J. Am. Ceram. Soc. 93 (2010) 2121–2124, https://doi.org/10.1111/j.1551-2916.2010.03673.x.

[28] E. Oz, S. Demirel, S. Altin, E. Altin, O. Baglayan, A. Bayri, S. Avci, Fabrication of Ca-Mn-Nb-O compounds and their structural, electrical, magnetic and thermoelectric properties, Mater. Res. Express 5 (2018) 036304, https://doi.org/10.1088/2053-1591/aab3af.

[29] A. Mishra, S. Bhattacharjee, Effect of A- or B-site doping of perovskite calcium manganite on structure, resistivity, and thermoelectric properties, J. Am. Ceram. Soc. 100 (2017) 4945–4953, https://doi.org/10.1111/jace.15015.

[30] S.H. Chun, M.B. Salamon, Y. Lyanda-Geller, P.M. Goldbart, P.D. Han, Magnetotransport in Manganites and the role of quantal phases: theory and experiment, Phys. Rev. Lett. 84 (2000) 757–760, https://doi.org/10.1103/PhysRevLett.84.757.

[31] G. Jakob, W. Westerburg, F. Martin, H. Adrian, Small-polaron transport in La0.67Ca0.33MnO3 thin films, Phys. Rev. B 58 (1998) 14966–14970, https://doi.org/10.1103/PhysRevB.58.14966.

[32] D. Flahaut, T. Mihara, R. Funahashi, N. Nabeshima, K. Lee, H. Ohta, K. Koumoto, Thermoelectrical properties of A -site substituted Ca1-xrexMnO3 system, J. Appl. Phys. 100 (2006) 084911, https://doi.org/10.1063/1.2362922.

[33] P. Kumar, S.C. Kashyap, V.K. Sharma, H.C. Gupta, Improved thermoelectric property of cation-substituted CaMnO3, Chin. Phys. B 24 (2015) 098101, https://doi.org/10.1088/1674-1056/24/9/098101.

[34] M. Mouyane, B. Itaalit, J.O. Bernard, D. Houivet, J.G. Noudem, Flash combustion synthesis of electron doped-CaMnO3 thermoelectric oxides, Powder Technol. 264 (2014) 71–77, https://doi.org/10.1016/j.powtec.2014.05.022.

[35] Y.C. Zhou, C.L. Wang, W.B. Su, J. Liu, H.C. Wang, J.C. Li, Y. Li, J.Z. Zhai, Y. C. Zhang, L.M. Mei, Electrical properties of Dy3+/Na+ Co-doped oxide thermoelectric [Ca1-x(Na1/2Dy1/2)x]MnO3 ceramics, J. Alloys Compd. 680 (2016) 129–132, https://doi.org/10.1016/j.jallcom.2016.04.158.

[36] D. Flahaut, J. Allouche, A. Sotelo, Sh. Rasekh, M.A. Torres, M.A. Madre, J.C. Diez, Role of Ag in textured-annealed Bi2Ca2Co1.7Ox thermoelectric ceramic, Acta Mater. 102 (2016) 273–283, https://doi.org/10.1016/j.actamat.2015.09.036.

[37] M. Cutler, J.F. Leavy, R.L. Fitzpatrick, Electronic transport in semimetallic cerium sulfide, Phys. Rev. 133 (1964) A1143–A1152, https://doi.org/10.1103/PhysRev.133.A1143.

[38] A. Sotelo, P. Amirkhizi, O.J. Dura, G. García, A.C. Asensio, M.A. Torres, M. A. Madre, A. Kovalevsky, Sh Rasekh, Significant reduction in processing time for Ca0.95Ce0.05MnO3 thermoelectric ceramics, Ceram. Int. 49 (2023) 37793–37799, https://doi.org/10.1016/j.ceramint.2023.09.107.

[39] Y.H. Zhu, W.B. Su, Y.C. Zhou, J. Li, X. Zhang, J. Du, C.L. Wang, Effects of Dy and Yb co-doping on thermoelectric properties of CaMnO3 ceramics, Ceram. Int. 41 (2015) 1535–1539, https://doi.org/10.1016/j.ceramint.2014.09.089.

[40] C. Wang, L. Shi, X. Xu, S. Zhou, J. Zhao, Y. Guo, H. Liu, L. He, X. Cai, G. Xu, High-temperature thermoelectric characteristics of B-site substituted Yb0.1Ca0.9Mn1-xNbxO3 system (0≤x≤0.1), Appl. Phys. A 112 (2013) 1003–1009, https://doi.org/10.1007/s00339-012-7465-6.

[41] N.M. Ferreira, N.R. Neves, M.C. Ferro, M.A. Torres, M.A. Madre, F.M. Costa, A. Sotelo, A.V. Kovalevsky, Growth rate effects on the thermoelectric performance of CaMnO3-based ceramics, J. Eur. Ceram. Soc. 39 (2019) 4184–4188, https://doi.org/10.1016/j.jeurceramsoc.2019.06.011.

[42] K.K. Liu, Z.Y. Liu, F.P. Zhang, X.Y. Zhang, J.W. Zhang, J.L. Shi, G. Ren, T.W. He, J. J. Duan, Improved thermoelectric performance in Pr and Sr Co-doped CaMnO3

materials, J. Alloys Compd. 808 (2019), https://doi.org/10.1016/j.jallcom.2019.07.188.

[43] G. Xu, R. Funahashi, I. Matsubara, M. Shikano, Y. Zhou, High-temperature thermoelectric properties of the $Ca_{1-x}Bi_xMnO_3$ system, J. Mater. Res. 17 (2002) 1092–1095, https://doi.org/10.1557/JMR.2002.0161.

[44] T. Chen, J. Wang, X. Wang, H. Wang, W. Su, J. Zhai, F. Mehmood, M. Khan, C. Wang, Cross-scale porous structure design leads to optimized thermoelectric performance and high output power for $CaMnO_3$ ceramics and their uni-leg modules, Appl. Mater. Today 29 (2022) 101557, https://doi.org/10.1016/j.apmt.2022.101557.

[45] S.P. Singh, N. Kanas, T.D. Desissa, M.A. Einarsrud, T. Norby, K. Wiik, Thermoelectric properties of non-stoichiometric $CaMnO_{3-\delta}$ composites formed by redox-activated exsolution, J. Eur. Ceram. Soc. 40 (2020) 1344–1351, https://doi.org/10.1016/j.jeurceramsoc.2019.11.027.

[46] S.P. Singh, N. Kanas, M.A. Einarsrud, K. Wiik, The effect of alkaline earth metal substitution on thermoelectric properties of $A_{0.98}La_{0.02}MnO_{3-\delta}$ (A = Ca, Ba), Process. Appl. Ceram. 16 (2022) 78–82, https://doi.org/10.2298/PAC2201078S.

[47] T. Wang, P. Nan, H.C. Wang, W. Su, A. Sotelo, J. Zhai, X. Wang, Y. Ran, T. Chen, C. L. Wang, Right heterogeneous microstructure for achieving excellent thermoelectric performance in $Ca_{0.9}R_{0.1}MnO_{3-\delta}$ (R=Dy, Yb) ceramics, Inorg. Chem. 57 (2018) 9133–9141, https://doi.org/10.1021/acs.inorgchem.8b01163.

[48] K.K. Liu, Z.Y. Liu, F.P. Zhang, J.X. Zhang, X.Y. Yang, J.W. Zhang, J.L. Shi, G. Ren, T.W. He, J.J. Duan, Improved thermoelectric performance in Pr and Sr Co-doped $CaMnO_3$ materials, J. Alloys Compd. 808 (2019) 151476, https://doi.org/10.1016/j.jallcom.2019.07.188.

[49] D. Srivastava, F. Azough, R. Freer, E. Combe, R. Funahashi, D.M. Kepaptsoglou, Q. M. Ramasse, M. Molinari, S.R. Yeandel, J.D. Baran, S.C. Parker, Crystal structure and thermoelectric properties of Sr–Mo substituted $CaMnO_3$: a combined experimental and computational study, J. Mater. Chem. C 3 (2015) 12245–12259, https://doi.org/10.1039/c5tc02318a.

[50] M. Ohtaki, H. Koga, T. Tokunaga, K. Eguchi, H. Arai, Electrical transport properties and high-temperature thermoelectric performance of $(Ca_{0.9}M_{0.1})MnO_3$ (M= Y, La, Ce, Sm, In, Sn, Sb, Pb, Bi), J. Solid State Chem. 120 (1995) 105–111, https://doi.org/10.1006/jssc.1995.1384.

[51] A. Bhaskar, C. Liu, J. Yuan, Thermoelectric and magnetic properties of $Ca_{0.98}re_{0.02}MnO_{3-\delta}$ (Re=Sm, Gd and Dy), J. Electron. Mater. 41 (2012) 2338–2344, https://doi.org/10.1007/s11664-012-2159-6.

[52] M. Molinari, D.A. Tompsett, S.C. Parker, F. Azough, R. Freer, Structural, electronic and thermoelectric behavior of $CaMnO_3$ and $CaMnO_{(3-\delta)}$, J. Mater. Chem. A 2 (2014) 14109–14117, https://doi.org/10.1039/c4ta01514b.

[53] Y. Wang, Y. Sui, H. Fan, X. Wang, W. Su, X. Liu, High temperature thermoelectric response of electron-doped $CaMnO_3$, Chem. Mater. 21 (2009) 4653–4660, https://doi.org/10.1021/cm901766y.

[54] X. Song, S.A.P. Navia, L. Liang, C. Boyle, C.O. Romo-De-La-Cruz, B. Jackson, A. Hinerman, M. Wilt, J. Prucz, Y. Chen, Grain boundary phase segregation for dramatic improvement of the thermoelectric performance of oxide ceramics, ACS Appl. Mater. Interfaces 10 (2018) 39018–39024, https://doi.org/10.1021/acsami.8b12710.

[55] M. Wolf, R. Hinterding, A. Feldhoff, High power factor vs. High zT—A review of thermoelectric materials for High-temperature application, Entropy 21 (2019) 1058, https://doi.org/10.3390/e21111058.